Vietnam Journal of Catalysis and Adsorption
Tạp chí xúc tác và hấp phụ Việt Nam

https://jca.edu.vn

Facile synthesis of ultrasmall Bi_2O_3 nanoparticles for computed tomography imaging

Le Thi Thanh Tam[1,*], Nguyen Thi Yen[1], Duong Thi Ngoc[3], Ha Minh Nguyet[1,2], Hoang Tran Dung[1], Ngo Ba Thanh[1], Nguyen Tuan Dung[1], Ngo Thanh Dung[1], Le Trong Lu[1,2,*]

[1] *Institute of Materials Science, Vietnam Academy of Science and Technology, 18 Hoang Quoc Viet Road, Hanoi, VIETNAM.*
[2] *Graduate University of Science and Technology, Vietnam Academy of Science and Technology, 18 Hoang Quoc Viet Road, Hanoi, VIETNAM.*
[3] *Hanoi National University of Education, 136 Xuan Thuy Road, Hanoi, VIETNAM.*
** Email: thanhtam.le95pt@gmail.com, lult@ims.vast.ac.vn*

ARTICLE INFO

Received: 11/11/2025
Accepted: 26/11/2025
Issue date: 30/12/2025

Keywords:
Bi_2O_3 nanoparticles;
Polyacrylic acid coating;
polyol synthesis;
X-ray attenuation;
CT contrast agent

ABSTRACT

Ultrasmall bismuth oxide nanoparticles (Bi_2O_3 NP) are emerging as promising CT contrast agents owing to their high atomic number, strong X-ray attenuation, and versatile surface chemistry. Herein, we report a facile one-pot polyol synthesis of Bi_2O_3 NPs using triethylene glycol and polyacrylic acid (PAA), which acts as both surfactant and biocompatible coating. The obtained Bi_2O_3@PAA NPs exhibit an average core size of ~4.4 nm, uniform dispersion, and excellent aqueous stability. Their structural and surface characteristics were comprehensively confirmed by TEM, XRD, DLS, FTIR and TGA analyses. In vitro CT imaging experiments demonstrated that Bi_2O_3@PAA NPs produced a linear and concentration-dependent enhancement in Hounsfield units (HU), achieving an X-ray attenuation efficiency significantly higher than that of the commercial iodine-based contrast agent iobitridol under identical conditions. These findings highlight the potential of ultrasmall Bi_2O_3@PAA NPs as next-generation CT contrast agents.

Introduction

Computed tomography (CT) is a powerful imaging technique that provides high spatial resolution, rapid acquisition, and clear three-dimensional visualization of anatomical structures [1,2]. To further enhance image contrast and delineate specific tissues or lesions, contrast agents are often administered [3]. However, conventional iodine-based agents (e.g., iobitridol, iohexol) exhibit low X-ray attenuation (Z = 53), short circulation time, and potential nephrotoxicity at high doses [4–6]. These limitations have motivated the exploration of alternative contrast agents composed of elements with higher atomic numbers, which can offer stronger X-ray attenuation and improved imaging efficiency for CT applications.

Among high-Z elements, bismuth (Z = 83) has attracted great attention due to its exceptionally high X-ray attenuation coefficient, chemical stability, and relatively low toxicity compared with other heavy metals [7-9]. Various bismuth-based nanostructures, including Bi, Bi_2S_3 and Bi_2O_3, have been investigated as potential CT contrast agents owing to their strong attenuation capability and versatile chemical tunability [10-12]. In particular, bismuth oxide nanoparticles (Bi_2O_3 NPs) are highly promising because of their high density

https://doi.org/10.62239/jca.2025.062

(8.9 g/cm^3), strong X-ray absorption, and facile synthesis [9,13]. However, conventional Bi_2O_3 NPs often exhibit large particle sizes and poor dispersibility in aqueous media, leading to aggregation and reduced imaging performance [14,15].

To overcome these limitations, the design of ultrasmall Bi_2O_3 NPs with sizes below 10 nm has gained increasing interest. Such nanoparticles provide superior colloidal stability, uniform distribution, and more homogeneous attenuation within biological systems [16]. Nevertheless, synthesizing ultrasmall and monodisperse Bi_2O_3 NPs remains challenging because most conventional routes require harsh conditions or complex surface modifications to achieve size control and stability [12]. Therefore, developing a simple and reliable method for preparing ultrasmall Bi_2O_3 NPs with strong X-ray attenuation is highly desirable for advancing CT imaging technology.

In this study, we report a simple and efficient route for the synthesis of ultrasmall Bi_2O_3 NPs with an average diameter of approximately 4.4 nm. The obtained NPs exhibit uniform morphology and excellent aqueous dispersibility. CT phantom imaging revealed a high X-ray attenuation coefficient of 12.96 HU/mM, more than twice that of the commercial iodine-based contrast agent iobitridol (5.45 HU/mM). These findings demonstrate that ultrasmall Bi_2O_3 NPs synthesized via a facile method can serve as efficient, iodine-free CT contrast agents for next-generation imaging applications.

Experimental

Chemical

All chemicals were of high purity and used as received without further purification. Bismuth nitrate pentahydrate ($Bi(NO_3)_3.5H_2O$, 98%), triethylene glycol (TEG, 99.8%), polyacrylic acid (PAA, MW = 1800), sodium hydroxide (NaOH, 98%) and absolute ethanol were purchased from Sigma-Aldrich, Ltd. Double-distilled water was throughout the experiments.

Synthesis of Bi_2O_3@PAA NPs

Ultrasmall Bi_2O_3@PAA NPs were prepared through a one-pot polyol method. Briefly, 10 mmol of $Bi(NO_3)_3.5H_2O$ was dissolved in 40 mL of TEG containing 1.8 g of PAA in a 100 mL three-neck flask under magnetic stirring until complete dissolution. The solution was then heated to 80 °C, followed by the addition of 1.2 g of NaOH dissolved in 10 mL of preheated TEG (80 °C). The resulting mixture was gradually heated to 140 °C and maintained at this temperature for 12 hours under a continuous nitrogen flow. After natural cooling to room temperature, the obtained Bi_2O_3@PAA NPs were separated by centrifugation, thoroughly washed with deionized water and absolute ethanol several times to remove unreacted species, and finally redispersed in distilled water to achieve a concentration of 10 mg/mL.

Characterization

Transmission electron microscopy (TEM, JEM1010, JEOL) was used to observe particle size and morphology. The crystalline structure and phase composition were characterized using X-ray diffraction (XRD) with Cu Kα radiation. The elemental composition and distribution was analyzed by energy dispersive X-ray spectroscopy (EDS) mapping (Hitachi S-4800 FESEM), while the Bi content was quantified by inductively coupled plasma mass spectrometry (ICP–MS, Agilent). Fourier-transform infrared spectroscopy (FTIR, Nicolet 6700) and thermogravimetric analysis (TGA, Netzsch, Germany) were employed to verify the presence of PAA coating. Dynamic light scattering (DLS) and zeta potential measurements were conducted to evaluate the hydrodynamic particle size and colloidal stability.

CT phantom imaging

In vitro CT imaging was conducted using a 128-slice Somatom Perspective scanner (Siemens, Germany). Bi_2O_3@PAA NP suspensions containing different Bi concentrations (1.06, 2.13, 3.18, 4.25, and 8.50 mM) were prepared in 2% agarose gel and scanned at tube voltages of 80–130 kV. X-ray attenuation values (HU) were obtained from regions of interest (ROI) using eFilm software (Merge Healthcare, Chicago, IL, USA). Iobitridol (Xenetix 300) solutions with equivalent iodine concentrations were used as controls.

Results and discussion

Characterization of Bi_2O_3@PAA NPs

In this work, the successful synthesis of ultrasmall Bi_2O_3@PAA NPs via the one-pot polyol method was confirmed through a series of complementary characterization techniques. These analyses consistently demonstrated the formation of Bi_2O_3 cores stabilized by a PAA shell. The procedure yielded over 70% with excellent batch-to-batch reproducibility, demonstrating the robustness of the method. Based on the precursor chemistry and reaction conditions, the formation mechanism of Bi_2O_3@PAA NPs can be proposed as follows:

$$Bi^{3+}(aq) + 3OH^-(aq) + PAA\ (aq) \rightarrow PAA\text{-}Bi(OH)_3\ (aq)$$

$$PAA\text{-}Bi(OH)_3\ (aq) \rightarrow PAA\text{-}Bi_2O_3(aq) + H_2O$$

https://doi.org/10.62239/jca.2025.062

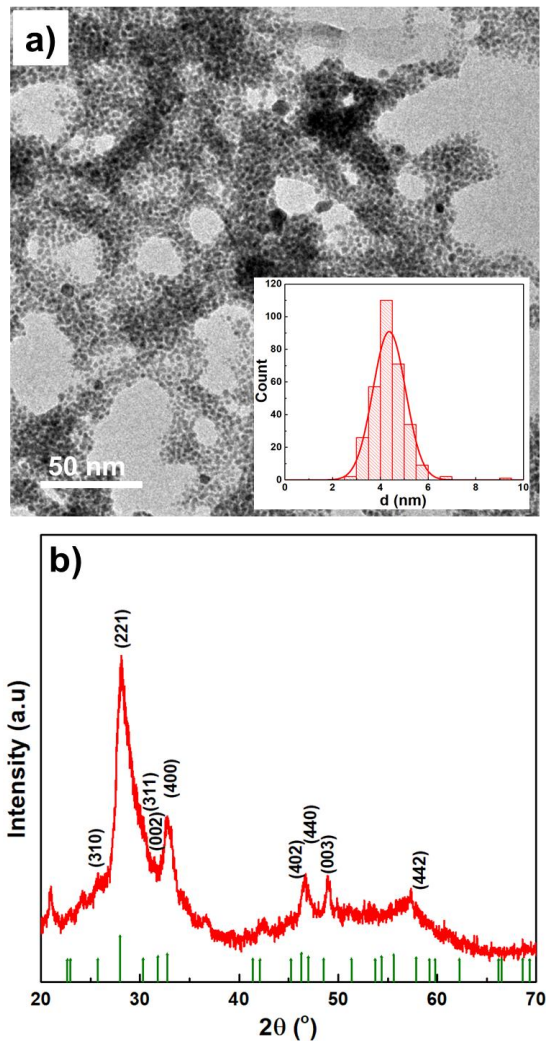

Fig 1: a) TEM image and particle size distribution histogram (inset), b) XRD pattern of Bi_2O_3@PAA NPs.

The morphology and size distribution of the Bi_2O_3@PAA NPs were characterized by transmission electron microscopy (TEM), as shown in Fig 1a. The nanoparticles exhibit a nearly spherical shape with uniform size distribution, indicating the effective stabilizing role of the PAA coating. The particle size histogram (inset of Fig 1a) reveals a narrow size distribution centered at approximately 4.4 ± 0.7 nm, confirming the formation of ultrasmall NPs.

The ultrasmall size of Bi_2O_3 NPs arises from the critical role of PAA during the nucleation and growth process. Strong coordination between the carboxylate groups of PAA and Bi^{3+} ions forms stable PAA-$Bi(OH)_3$ complexes, reducing free Bi^{3+} and limiting uncontrolled growth. Additionally, PAA chains provide steric and electrostatic barriers that prevent particle coalescence in the polyol medium. These effects restrict particle growth, inhibit agglomeration, and produce well-dispersed ultrasmall Bi_2O_3 cores.

The crystalline structure of the Bi_2O_3@PAA NPs was further examined using X-ray diffraction (XRD), as presented in Fig 1b. The diffraction peaks located at 2θ = 25.7°, 28.0°, 32.8°, 46.3°, 46.9°, and 57.6° correspond well to the (310), (221), (400), (402), (003), and (442) planes of tetragonal β-Bi_2O_3 (JCPDS No. 74-1374) [12]. No additional peaks from metallic Bi or other bismuth oxides were observed, indicating high phase purity. The broadening of diffraction peaks reflects the nanoscale crystallite size, consistent with the TEM analysis [17]. The stabilization of the β-phase is beneficial for CT imaging applications, as its tetragonal structure provides higher local electron density and more efficient atomic packing around Bi atoms. These features enhance the probability of photoelectric interactions with X-rays, leading to an increased attenuation coefficient. Consequently, the Bi_2O_3@PAA NPs exhibit stronger X-ray attenuation, emphasizing the importance of phase control in optimizing the contrast performance of Bi-based nanomaterials.

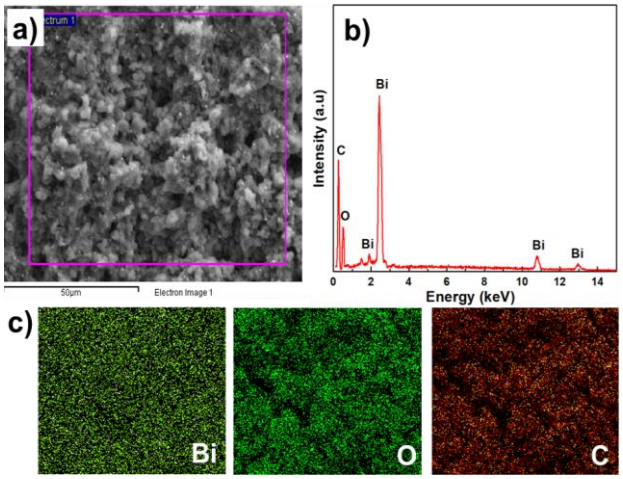

Fig 2: a) SEM image, b) EDS spectrum and c) EDS mapping of Bi_2O_3@PAA NPs.

The elemental composition of the synthesized Bi_2O_3@PAA NPs was analyzed by energy-dispersive X-ray spectroscopy (EDS), as shown in Fig 2. The EDS spectrum displayed characteristic peaks of Bi and O, confirming the formation of Bi_2O_3. A weak carbon signal was also observed, which originated from the PAA coating layer on the nanoparticle surface and contributed to their excellent aqueous dispersibility. Furthermore, the EDS elemental mapping revealed a uniform spatial distribution of Bi, O, and C elements across the entire sample, indicating homogeneous composition and effective surface modification. The absence of additional impurity signals demonstrates the high purity of the synthesized Bi_2O_3@PAA NPs.

https://doi.org/10.62239/jca.2025.062

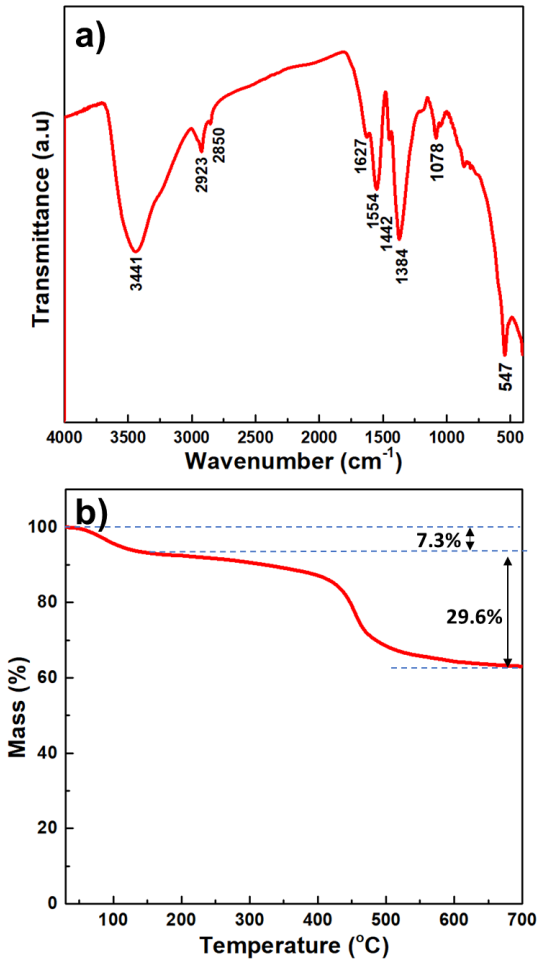

Fig 3: a) FTIR spectrum and b) TGA curve of Bi_2O_3@PAA NPs.

The FTIR spectrum of Bi_2O_3@PAA NPs (Fig 3a) further verified the successful surface modification by polyacrylic acid (PAA). The broad absorption band at 3341 cm^{-1} is assigned to the stretching vibration of O-H groups, whereas the peaks at 2923 and 2850 cm^{-1} correspond to the C-H stretching vibrations of the -CH_2- groups in PAA. The absorption bands at 1627, 1554, and 1442 cm^{-1} are associated with asymmetric and symmetric stretching vibrations of the carboxylate ($-COO^-$) groups, indicating the coordination of PAA molecules to the Bi_2O_3 surface through bidentate or bridging modes. The peak at 1384 cm^{-1} corresponds to C-O stretching, and the band at 1078 cm^{-1} is related to C-O-C stretching vibrations of the polymer backbone. Notably, the characteristic Bi-O stretching vibration observed at around 547 cm^{-1} confirms the presence of Bi_2O_3 as the inorganic core [12,18]. These features collectively demonstrate that PAA molecules were successfully anchored onto the surface of Bi_2O_3 NPs, providing functional carboxyl groups that enhance colloidal stability in water.

The thermal stability and organic content of Bi_2O_3@PAA nanoparticles were investigated by thermogravimetric analysis (TGA) (Fig 3b). The TGA curve exhibited two major weight-loss steps. The initial loss of approximately 7.3% below 150 °C is attributed to the evaporation of physically adsorbed water and residual solvent molecules. The second weight-loss stage, occurring between 200 °C and 600 °C with a mass decrease of about 29.6%, corresponds to the thermal decomposition of the PAA coating layer. The remaining stable fraction represents the inorganic Bi_2O_3 core, confirming the successful coating of a polymer shell on the nanoparticle surface.

Dynamic light scattering (DLS) measurements were performed to evaluate the hydrodynamic size and colloidal stability of the Bi_2O_3@PAA NPs in aqueous dispersion. The DLS spectrum (Fig 4a) revealed a narrow and monomodal size distribution with an average hydrodynamic diameter of approximately 118.3 nm, which is larger than the core size observed in TEM images (~4.4 nm). This difference is primarily due to the presence of the polymeric PAA coating, which forms a hydrated and extended shell around each nanoparticle, as well as the potential formation of soft agglomerates arising from weak, reversible interparticle interactions in solution [19]. The dynamic and flexible nature of the polymer chains further contributes to the increased hydrodynamic size. Despite this enlargement, the narrow and uniform distribution with a relatively low PDI (PDI = 0.324) indicates that the PAA surface modification effectively prevents hard aggregation, maintaining good colloidal stability in aqueous media.

The zeta potential measurement further confirmed the excellent colloidal stability of Bi_2O_3@PAA NPs, showing a strongly negative surface potential of -32.2 mV (Fig 4b). The high negative value arises from the deprotonation of carboxyl ($-COO^-$) groups on the PAA chains at neutral pH, which generates strong electrostatic repulsion between nanoparticles. Such a surface charge not only stabilizes the colloidal system against aggregation but also provides active sites for potential bioconjugation. Besides, its hydrophilic and negatively charged shell reduces non-specific protein adsorption, potentially prolonging circulation *in vivo*, while the ultrasmall size and polymer coating facilitate gradual renal and hepatobiliary clearance of the NPs. These results demonstrate that PAA effectively enhances the aqueous dispersibility and stability of Bi_2O_3 NPs, making them suitable for further biomedical applications such as CT imaging.

https://doi.org/10.62239/jca.2025.062

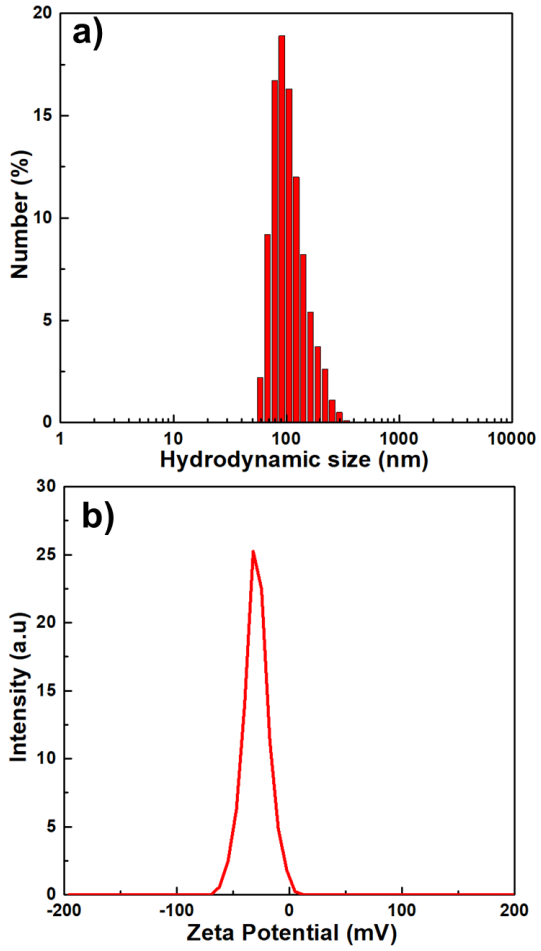

Fig 4: a) DLS spectrum and b) Zeta potential of Bi_2O_3@PAA NPs

In vitro CT imaging performance

The X-ray attenuation performance of Bi_2O_3@PAA NPs was evaluated by computed tomography (CT) imaging at different X-ray tube voltages (80, 110, and 130 kV). As shown in Fig 5a, the CT signal intensity exhibited a concentration-dependent enhancement, indicating that the attenuation ability of the Bi_2O_3@PAA NPs increases with Bi concentration. The linear fitting of Hounsfield unit (HU) values versus Bi concentration yielded high correlation coefficients (R^2 > 0.99), confirming the reliability of the quantitative analysis.

The measured X-ray attenuation coefficients of Bi_2O_3@PAA NPs were 12.96, 12.63, and 11.54 HU/mM at 80, 110, and 130 kV, respectively (Fig 5b). In comparison, the clinical iodine-based contrast agent iobitridol exhibited significantly lower attenuation values of 5.45, 4.21, and 3.48 HU/mM under the same conditions. These results clearly demonstrate that Bi_2O_3@PAA NPs provide superior X-ray attenuation efficiency across all tested energy levels. The enhanced attenuation capability can be attributed to the high atomic number (Z = 83) and large X-ray absorption cross-section of bismuth, which enables more effective photon absorption compared to iodine (Z = 53). Furthermore, the X-ray attenuation coefficient of Bi_2O_3@PAA NPs is higher than those reported for previously studied Bi-based contrast agents [20,21], indicating an improvement in attenuation efficiency over earlier Bi-based systems.

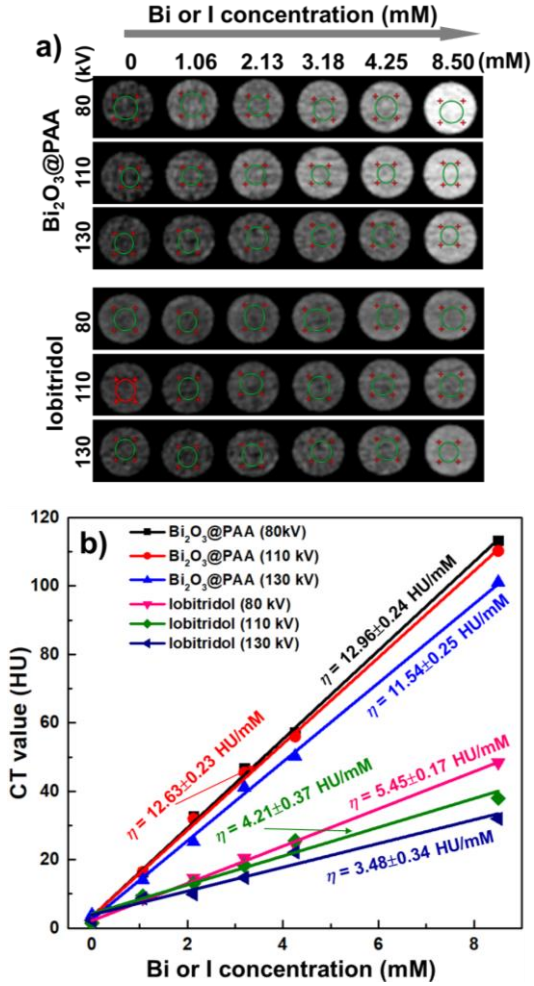

Fig 5: a) *In vitro* CT imaging and b) CT signals curves of Bi_2O_3@PAA NPs and clinical iobitridol as a function of the Bi or I concentration under different tube voltage of 80, 110 and 130 kV. (ROI ≈ 0.3 cm^2)

Moreover, the gradual decrease in HU values with increasing tube voltage is consistent with the energy-dependent attenuation behavior typical of high-Z elements, in which the photoelectric absorption effect dominates at lower photon energies [12]. This trend further confirms that the X-ray attenuation of Bi_2O_3@PAA NPs follows the expected physical mechanism for heavy-element-based CT contrast agents. Collectively, these findings indicate that Bi_2O_3@PAA NPs exhibit excellent X-ray attenuation performance and hold great promise as a highly

https://doi.org/10.62239/jca.2025.062

efficient CT contrast agent, outperforming conventional iodine-based formulations in both sensitivity and signal intensity.

This study focuses exclusively on evaluating X-ray attenuation performance of Bi_2O_3@PAA NPs and no assessments of cytotoxicity, hemocompatibility, or *in-vivo* biosafety were conducted. Therefore, comprehensive biological evaluations, including cytotoxicity, hemolysis, degradation behavior, and pharmacokinetics, will be carried out in future studies to establish their safety for biomedical applications.

Conclusion

In this study, we developed ultrasmall, water-dispersible Bi_2O_3@PAA NPs (~4.4 nm) with excellent colloidal stability using a simple one-pot polyol method. The nanoparticles exhibited markedly enhanced X-ray attenuation compared with conventional iodine-based contrast agents, highlighting the importance of controlled particle size and surface functionalization for improved CT imaging performance. While the current work focuses on imaging efficiency, comprehensive evaluations of biosafety, including cytotoxicity, hemocompatibility, biodistribution, and clearance, will be conducted in future studies. In addition, surface optimization and evaluation in *in vivo* models will be explored to further enhance biocompatibility, circulation time, and diagnostic applicability. These efforts will help establish Bi_2O_3@PAA NPs as a promising next-generation CT contrast platform.

Acknowledgments

This research was financially supported by the Development program in the Field of Physics for the 2021-2025 period, through the Ministry of Science and Technology of Vietnam (Grant number: ĐTĐLCN16/23). The authors thank Le The Tam for valuable assistance with the CT imaging measurements.

References

1. H. Lusic, M.W. Grinstaff, Chem. Rev. 113(3) (2013) 1641–1666. https://doi.org/10.1021/cr200358s
2. J. Hsieh, T. Flohr, J. Med. Imag. 8(5) (2021) 052109. https://doi.org/10.1117/1.JMI.8.5.052109
3. H. Sbitany, P.F. Koltz, C. Mays, J.A. Girotto, H.N. Langstein, Int. J. Surg. 8 (2010) 384–386. https://doi.org/10.1016/j.ijsu.2010.06.002
4. T.C. Owens, N. Anton, M.F. Attia, Acta Biomaterialia, 171 (2023) 19–36. https://doi.org/10.1016/j.actbio.2023.09.027
5. N. Gharehaghaji, B. Divband, F. Bakhtiari-Asl. BioNanoScience 10 (2020) 909–916. https://doi.org/10.1007/s12668-020-00787-1
6. M. Yektamanesh, Y. Ayyami, M. Ghorbani, M. Dastgir, R. Malekzadeh, T. Mortezazadeh, Int. J. Pharm. 659 (2024) 124264. https://doi.org/10.1016/j.ijpharm.2024.124264
7. I. Mutreja, N. Maalej, A. Kaushik, D. Kumar, A. Raja, Mater. Adv. 4 (2023) 3967-3988. https://doi.org/10.1039/D3MA00231D
8. M.Y. Ahmad, S. Liu, T. Tegafaw, A.K.A.A. Saidi, D. Zhao, Y. Liu, S.W. Nam, Y. Chang, G.H. Lee, Pharmaceuticals 16(10) (2023) 1463. https://doi.org/10.3390/ph16101463
9. A. Ghazanfari, S. Marasini, X. Miao, J.A. Park, K.-H. Jung, M.Y. Ahmad, H. Yue, S.L. Ho, S. Liu, Y.J. Jang, K.S. Chae, Y. Chang, G.H. Lee, Colloids Surf. A: Physicochem. Eng. Asp. 576 (2019) 73–81. https://doi.org/10.1016/j.colsurfa.2019.05.033
10. A.L. Brown, P.C. Naha, V. Benavides-montes, H.I. Litt, A.M. Goforth, D.P. Cormode, Chem. Mater. 26 (2014) 2266–2274. https://doi.org/10.1021/cm500077z
11. G. Shu, C. Zhang, Y. Wen, J. Pan, X. Zhang, S.K. Sun, Biomaterials 311 (2024) 122658. https://doi.org/10.1016/j.biomaterials.2024.122658
12. L.T.T. Tam, D.T. Ngoc, N.T.N. Linh, L.T. Tam, N.V. Dong, N.T. Yen, N.T. Suong, N.T. Dung, L.T. Lu, Nanoscale Adv. 7 (2025) 4183. https://doi.org/10.1039/D5NA00389J
13. R.M. El-Sharkawy, F.S. Abdou, M.A. Gizawy, E.A. Allam, M.E. Mahmoud, Radiat. Phys. Chem. 208 (2023) 110838. https://doi.org/10.1016/j.radphyschem.2023.110838
14. F. Du, J. Lou, R. Jiang, Z. Fang, X. Zhao, Y. Niu, S. Zou, M. Zhang, A. Gong, C. Wu, Int. J. Nanomed. 12 (2017) 5973–5992. https://doi.org/10.2147/IJN.S130455
15. A. Ghazanfari, S. Marasini, H. Yue, S.L. Ho, X. Miao, M.Y. Ahmad, J.A. Park, K.H. Jung, S. Liu, Y.J. Jang, K.S. Chae, Y. Chang, G.H. Lee, Int. J. Nanosci. Nanotechnol. 20 (2020) 4638. https://doi.org/10.1166/jnn.2020.17817
16. D. Zhao, A. Baek, T. Tegafaw, Y. Liu, S. Liu, H. Yue, E. Mulugeta, J. Yang, J.A. Park, H. Lee, D.W. Hwang, S. Kim, J. Kim, Y. Chang, G.H. Lee, ACS Appl. Nano Mater. 8 (2025) 13663-13675. https://doi.org/10.1021/acsanm.5c01443
17. A. Parbin, Rafiuddin, Mater. Adv. 3 (2022) 3316-3325. https://doi.org/10.1039/D1MA01254A
18. T. Placido, L. Tognaccini, B.D. Howes, A. Montrone, V. Laquintana, R. Comparelli, M.L. Curri, G. Smulevich, A. Agostiano, ACS Omega 3 (2018) 4959−4967. https://doi.org/10.1021/acsomega.8b00719.
19. D. Li, S. Wen, W. Sun, J. Zhang, D. Jin, C. Peng, M. Shen and X. Shi, ACS Appl. Bio Mater. 1(2) (2018) 221–225. https://doi.org/10.1021/acsabm.8b00265.
20. P. Lei, R. An, P. Zhang, S. Yao, S. Song, L. Dong, X. Xu, K. Du, J. Feng and H. Zhang, Adv. Funct. Mater. 27 (2017) 1702018. https://doi.org/10.1002/adfm.201702018
21. N. Yu, Z. Wang, J. Zhang, Z. Liu, B. Zhu, J. Yu, M. Zhu, C. Peng and Z. Chen, Biomaterials 161 (2018) 279-291. https://doi.org/10.1016/j.biomaterials.2018.01.047